Microstructure and compressive behavior of ice-templated copper foams with directional, lamellar pores

Hyeji Park[a], Myounggeun Choi[a], Heeman Choe[a,b,*], David C. Dunand[c]

[a] School of Materials Science and Engineering, Kookmin University, 77 Jeongneung-ro, Seongbuk-gu, Seoul 136-702, Republic of Korea
[b] Cellmotive Co. Ltd., Kookmin University, #518, Engineering Building, Seoul 136-702, Republic of Korea
[c] Department of Materials Science and Engineering, Northwestern University, 2220 Campus Drive, Evanston, IL 60208, USA

ARTICLE INFO

ABSTRACT

Copper foams are fabricated by directional freezing of aqueous suspensions of nanometric CuO powders followed by ice sublimation, reduction to Cu in Ar−5% H_2 gas and sintering. During slurry solidification, parallel, lamellar, centimeter-long ice dendrites grow, pushing the CuO powders into lamellar interdendritic spaces. Upon subsequent ice sublimation, the ice dendrites create lamellar pores surrounded by CuO walls that are subsequently reduced to copper and sintered; these ice-templated walls display surface micropores and, depending on the reduction/sintering parameters, internal micropores. Varying the main processing parameters – powder fraction in the slurry (from 13 to 19 vol%) and casting temperature (from −10 to −30 °C) – has a strong effect on the foam microstructure: (i) porosity (varying from 45% to 73%) is inversely related to slurry powder fraction, (ii) oriented lamellar macropores width increases from 15 to 64 μm with decreasing slurry fraction and increasing freezing temperature and (iii) oriented lamellar Cu wall width increases from 19 to 63 μm with increasing slurry fraction and freezing temperature. The resulting Cu foams show oriented, lamellar macropores (beneficial to permeability) and walls micropores (which increase the surface area) and are promising for use in electrochemical cells given the simplicity, scalability, low cost, and microstructure tunability associated with the ice-templating process. The ice-templated Cu foams, with pore directions parallel and perpendicular to the direction of compressive loading, show ductile compressive behavior with high yield stress, ductility and energy absorption; they are compared to model predictions and literature data of Cu lotus foams with elongated, cylindrical pores.

1. Introduction

Due to its excellent thermal and electrical conductivities, copper (Cu) is one of the most widely used materials for electrical applications [1,2]. Furthermore, porous Cu has generated recent interest for advanced electronic and energy devices owing to its high surface area, which is beneficial to rechargeable batteries, electrochemical catalyst, heat exchangers, heat pumps, fuel cells, and supercapacitors [3–10].

Cu foams can be manufactured through various methods including the space-holder technique [11], de-alloying (elimination of a less noble element in a binary copper alloy) [12], electrodeposition on fugitive scaffolds [13], sintering with generation of hydrogen bubbles [14], and freeze casting followed by sintering [2]. Because of its low cost and high potential for scalability, the freeze casting (ice templating) process is particularly promising. Freeze casting has been developed for producing porous ceramic materials [15] with complex shapes and fine features at low tooling cost. Freeze casting produces open

pores with interconnected channels or gradient pore sizes, with porosity as low as 25% and as high as 90% [16]. Freeze-cast materials also exhibit relatively high mechanical strength, can have elongated pores that are parallel to the ice front propagation, and can be tailored to form either homogeneous or directional microstructures [15,17]. However, this method was not used for producing porous metals until recently, because metallic powders tend to rapidly settle in a suspension and are generally susceptible to oxidation when exposed to water. Recently, Dunand and coworkers produced titanium foams with elongated pores by directional freeze casting Ti powder suspensions in water followed by sintering [18–20], as well as copper, iron and tungsten foams by directional freeze casting of CuO, Fe_2O_3 and WO_3 powder slurries, respectively, followed by hydrogen reduction and sintering [2,21,22].

The freeze-casting process is facile, scalable and economical, and thus of great interest for Cu foams as anode current collector in lithium-ion batteries where the porous architecture allows for volume
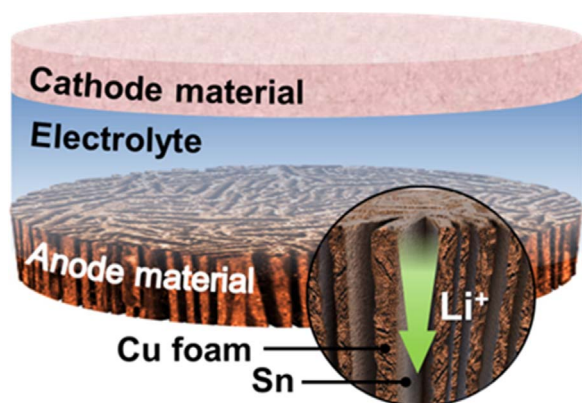
Fig. 1. Schematic of a lithium-ion battery design containing a freeze-cast Cu foam coated with Sn, with high permeability and open space to accommodate Sn (de)lithiation volume changes, which may be used as both the anode and current collector to enhance efficiency and cycling resistance during the (dis)charging process.

changes due to (de)lithiation [23]. Fig. 1 schematically shows that directionally freeze-cast Cu foam can be employed for anode current collectors of a lithium ion battery (LIB). In this design, the Cu foam, after being coated with an active material such as Si or Sn, is substituted for a Cu foil coated with an active powder material [3]. Si or Sn shows much higher electrochemical capacity than graphite but suffers from very high volumetric change (up to 300%) upon (de) lithiation, which can cause pulverization and loss of electrical contact at the electrode resulting in a rapidly decreasing anode capacity over multiple charge/discharge cycles. The well-aligned porous structure in a freeze-cast Cu foam current collector can accommodate the volume expansion/contraction during (de)lithiation enabling a better retention of the capacity of active anode materials. Moreover, owing to its anisotropic structural characteristics [24–29], a freeze-cast Cu foam has a number of practical benefits for use in electrochemical cells such as high specific surface area for high charging rate, fast gas transport for rapid electrochemical reaction, and high electrical conductivity. For example, one-dimensional TiO_2 structures have been used in solar cells to diminish charge recombination rates [29]. The aligned, elongated pores of directionally freeze-cast metallic foams also can provide efficient gas transport or ionic diffusion paths [24–28].

Recently, Ramos and Dunand [2] demonstrated production of copper foams with elongated pores by directionally ice-templated copper oxide (CuO) powder slurries followed by hydrogen reduction and sintering. Ran et al. [30] later showed that thermal decomposition from CuO to Cu was an alternative to achieving copper foams with equiaxed pores created by non-directional solidification of slurries. Although the article by Ramos and Dunand [2] was the first demonstration of ice-templated Cu foams, they did not carry out a systematic study of the effects of processing variables upon the foam microstructural morphology. The present study, therefore, focuses on the effects of the primary processing parameters in the freeze casting process (slurry CuO powder content, casting temperature, and sintering/ reduction conditions) on the morphology of Cu foams with a well-defined lamellar structure created by directional solidification. The compressive behavior of the Cu foams, with the load applied parallel or normal to the directional lamellar pores, is compared with theoretical models and experimental data on lotus Cu foams with long, aligned cylindrical pores usually fabricated by a unidirectional solidification method at a pressurized hydrogen or nitrogen gas with argon gas [47].

2. Experimental methods

Cupric oxide (CuO) powders (with particle size of 40–80 nm, purity of 99.9%, from Inframat Advanced Materials, Manchester, CT, USA) were suspended in a solution of 20 ml deionized water containing

2.5 wt% polyvinyl alcohol (PVA, Air Products and Chemicals Inc.). The slurry was sonicated for 1 h and stirred for 10 min, (repeated twice for complete particle dispersion), and then cooled to a few degrees above the freezing point of water. The cooled slurry was poured into a cylindrical mold consisting of insulating Teflon walls (37 and 45 mm inner- and outer-diameter) and a high-conductivity Cu base, consisting of a rod extending into an insulated steel container filled with ethyl alcohol cooled with an outer steel jacket containing liquid nitrogen. The temperature of the mold Cu base (i.e., the mold bottom surface) was controlled by a heating element wrapped around the Cu rod, using a thermocouple and temperature controller. Once the freezing process was completed, the frozen CuO-ice sample was removed from the mold and sublimated at −52 °C for 48 h in a freeze-dryer under 0.14 mbar residual pressure. The resulting green-body sample was then debinded, reduced from oxide to metal and sintered in a tube furnace under flowing Ar–5% H_2 gas at 800 °C for 6–8 h using heating and cooling rates of 5 °C min^{-1}. All but one samples were subjected to a reduction pre-heat treatment at 250 °C for 2 h prior to the 800 °C step, under flowing Ar–5% H_2 gas atmosphere.

In a first series of experiments, two slurries containing 12.5 vol% of the CuO powders in 20 ml deionized water were mixed with 2.5 wt% binder. The temperature of the mold bottom surface Cu base was fixed at −10 °C. After freeze-drying, one sample (labeled H1) was reduced and sintered in a single step at 800 °C for 6 h while the other sample (labeled H2) underwent a two-step heat-treatment (250 °C/2 h and 800 °C/6 h).

In a second series of experiments, the temperature of the mold bottom surface was varied (−10, −15, −20, and −30 °C) to observe the effect of solidification velocity on the morphology and structure of the pores for a fixed fraction of oxide powders in the slurries (12.5 vol%). The freeze-dried samples, labeled T10, T15, T20 and T35, respectively, were then subjected to the two-step heat-treatment (250 °C/2 h and 800 °C/6 h).

In a third series of experiments, the oxide powder fraction was varied (13, 14, 16, and 19 vol%) and the slurries were frozen at a constant mold bottom surface temperature of −15 °C. The freeze-dried samples, labeled V13, V14, V16 and V19 respectively, were then subjected to the two-step heat-treatment (250 °C/2 h and 800 °C/8 h).

Cross-sections of the foams were cut parallel to the longitudinal and transverse directions with respect to the temperature gradient, and examined by optical microscopy (PME 3, Olympus, Japan) and scanning electron microscopy (SEM, JSM7401F, JEOL, Japan); d their pore size, strut width, and total porosity were measured on optical images using the Image-Pro program. Some selected foams were further characterized via X-ray diffraction (XRD, MXP18A-HF, MAC Science, Tokyo, Japan), and atomic force microscopy (AFM, XE-100, Park System Corp., Republic of Korea) in contact mode to examine foam's surface morphology.

Uniaxial compression tests (Z020, Zwick GmbH & Co., Germany) were performed at room temperature at a nominal strain rate of 0.001 s^{-1} on two types of parallelepiped compression specimens (4 mm in diameter and 8 mm in height) with their longitudinal axis parallel (labeled V13P) or normal (labeled V13N) to the compressive loading direction.

3. Results and discussion

3.1. Foam microstructure

Fig. 2 shows photographs of a representative Cu foam (V13) before (left, 37 mm in diameter and 13 mm in height) and after (right, 21 mm in diameter and 6 mm in height) reduction and sintering under Ar−5% H_2; the figure illustrates a color change from black (oxide) to light red (metal) and the significant shrinkage (without cracking or warping) following binder removal, reduction and sintering. The volumetric shrinkage for this foam is ΔV/V ~85%, while the radial and height
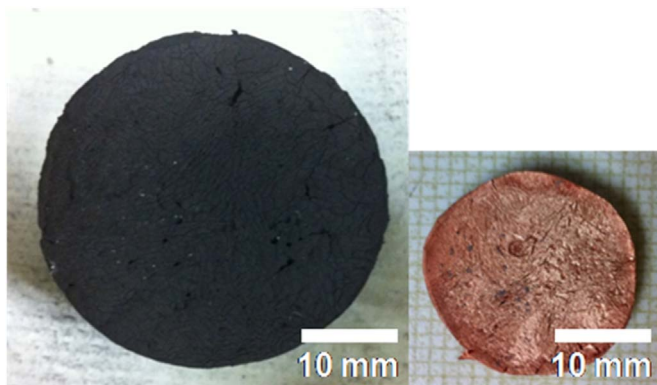
Fig. 2. Photographs of freeze-cast foam V13 after freeze drying (left) and after subsequent reduction and sintering (right), illustrating the color change from black CuO to light red Cu and considerable volume shrinkage without cracking or warping. (For interpretation of the references to color in this figure legend, the reader is referred to the web version of this article.)

shrinkages are $\Delta r/r$ ~43%, $\Delta h/h$ ~54%, respectively; thus shrinkage is near-isotropic, as also observed in a previous study [22].

Figs. 3 and 4 show respectively optical microscope and SEM images of two representative freeze-cast Cu foams (V13 and V14, respectively) created with nearly the same oxide volume fraction (12.5 and 13.7 vol %, respectively) and with the same −15 °C mold bottom temperature (described in the following as casting temperature). The micrographs show the expected morphology of colonies of aligned, lamellar macropore replicating ice dendrite colonies, whose directional growth during freezing result from the ~100–1000-fold higher growth velocity in the direction parallel, rather than perpendicular, to the temperature

gradient [31]. The aligned, lamellar macropores are surrounded by parallel Cu walls (28 µm in width) displaying micropores (~9 µm in size) on their surface (Figs. 3f and 4c). These surface micropores are present predominantly on one side of the Cu walls (indicated by circles in Figs. 3f and 4c), and result from the competition between the thermal and interfacial energies: the interfacial energy creates ice front tilted along a preferred direction with respect to the macroscopic thermal gradient direction [32–34]. Also, micropores are randomly distributed within the Cu walls, with equiaxed shape and an average size of 3 µm (Fig. 5a and b); they are likely due to incomplete sintering. X-ray diffraction (XRD) patterns for Cu foam (V14) after reduction and sintering exhibit peaks only at 43.3°, 50.4°, and 74.1°, all corresponding to pure metallic Cu, thus confirming full reduction of the cupric oxide powders.

Ten Cu foams were manufactured in this study, and their main processing parameters are summarized in Table 1. As seen in Table 1, by varying the slurry powder content, the casting temperature and the sintering profile, it is possible to modify, within relatively broad ranges, the pore fraction (from 45% to 73%), the lamellar pore width (from 15 to 64 µm), and the Cu wall width (from 19 to 63 µm), thus tailoring the foam's density, functional properties (e.g., permeability, surface area, thermal conductivity) and mechanical properties (e.g., stiffness, strength, energy absorption).

All but one foams showed high volume shrinkage (from 79% to 86%) as compared to the freeze-dried green bodies, resulting from binder removal, reduction of the powders from CuO to Cu, and their subsequent sintering into dense Cu walls surrounding the pores [22]. Only foam H1 showed lower shrinkage (47%), because of incomplete sintering as the reduction pre-heat treatment was not carried out, resulting in highly porous Cu walls as described in more details in the
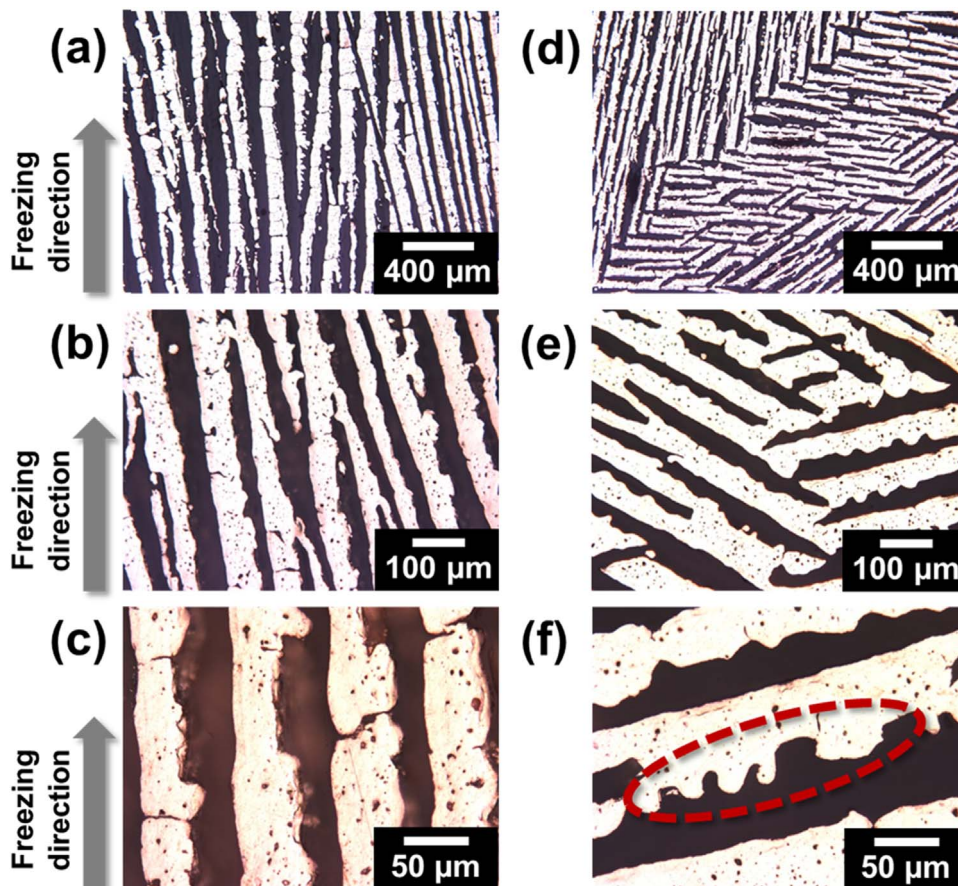

Fig. 3. Optical micrographs at various magnifications of Cu foam V13 showing (a, b, c) the lamellar macropore structure and (d, e, f) the morphology of the macropores and Cu walls, containing microporosity at their surface (circle) and, to a modest extent, within their volumes.
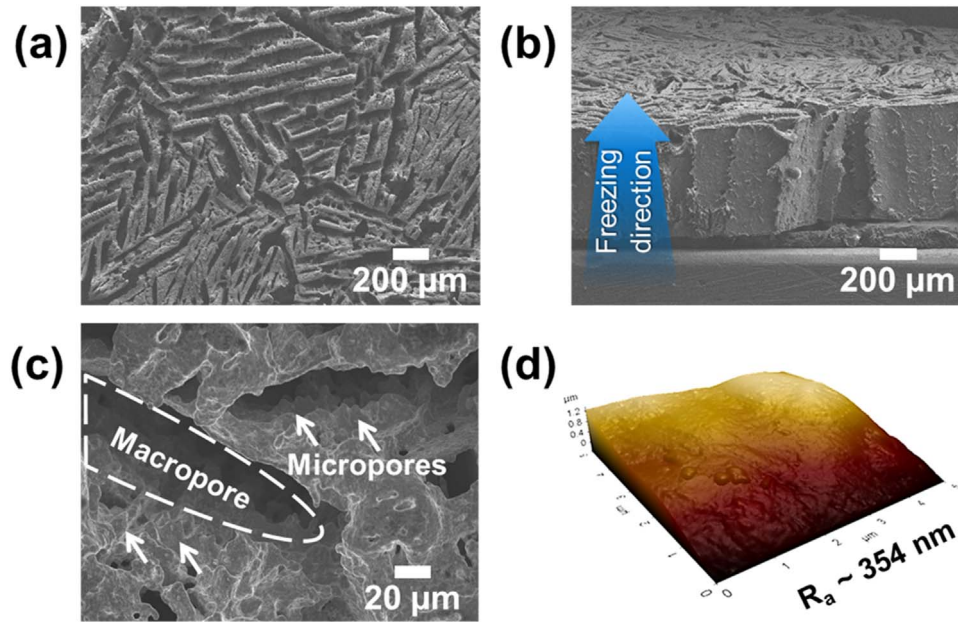
Fig. 4. SEM and AFM images of Cu foam V14 with a hierarchical pore structure: (a, b) lamellar macropores created by the ice dendrites during freezing, (c) micropores on the Cu walls, and (d) AFM image of the as-cast top morphology of the freeze-cast Cu foam with a mean surface roughness (R_a) ~350 nm.
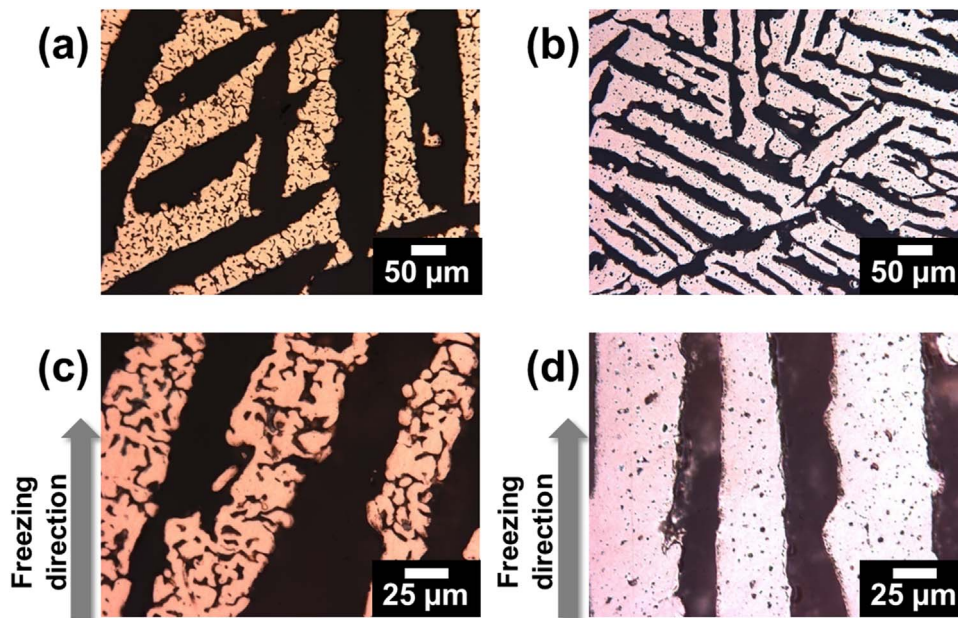

Fig. 5. Optical micrographs of cross-sections perpendicular (a, b) and parallel (c, d) directions to the freezing direction for Cu foams, created by freezing the same slurry (12.5 vol% CuO) at the same casting temperature (−10 °C), which were sintered at 800 °C for 8 h: (a, c) without reduction pre-heat treatment at 250 °C for 2 h (foam H1) and (b, d) with reduction pre-heat treatment at 250 °C for 2 h (foam H2). Differences in the micropore size and volume fraction on the walls surface, and within their volume, are visible.

Table 1

Overview of synthesized Cu-foams parameters listing the three main processing parameters (CuO volume fraction in the slurry f_{CuO}, casting temperature T_{cast}, sintering temperature T_{sinter}), and the four main foam microstructural parameters (foam volumetric shrinkage $\Delta V/V$, Cu wall thickness, macropore width and foam porosity).

Foam	f_{CuO} (vol%)	T_{cast} (°C)	T_{sinter} (°C)	Shrinkage $\Delta V/V$ (%)	Wall thickness (µm)	Macropore width (µm)	Porosity (%)
H1	12.5	−10	800	47	60 ± 10	64 ± 11	73
H2	”	”	250, 800	84	29 ± 3	51 ± 17	67
T10	12.5	−10	250, 800	84	29 ± 3	51 ± 17	67
T15	”	−15	”	85	27 ± 2	41 ± 5	67
T20	”	−20	”	”	19 ± 2	18 ± 2	67
T30	”	−30	”	86	20 ± 4	16 ± 2	63
V13	12.5	−15	250, 800	85	27 ± 7	41 ± 9	63
V14	13.7	”	”	78	28 ± 5	39 ± 8	58
V16	16.0	”	”	79	38 ± 6	33 ± 7	54
V19	19.2	”	”	81	63 ± 9	15 ± 5	45

following section.

Surface roughness of foam V14 was measured using AFM, as shown in Fig. 4d; a test spot was randomly selected for the AFM measurement out of the as-cast top surface of the Cu foam sample in Fig. 4d. A mean surface roughness (R_a) of ~350 nm was obtained, which is 4–9 times higher than the original oxide powder size (40–80 nm). Given that the average surface roughness of electroless deposited Cu film is reported as ~15 nm, the surface created in the freeze-cast Cu foam is ~ 25 times rougher [13]. The degree of surface roughness may be associated with the amount of surface area affecting charging rate and gas transport for electrochemical reaction when used for energy applications.

3.2. Effect of reduction pre-heat treatment

Fig. 5(a–d) show optical micrographs of polished Cu foams cross-sections taken in the directions perpendicular and parallel to the freezing direction, with and without the reduction pre-heat treatment at 250 °C. We could confirm that the 2 h reduction pre-heat treatment time at 250 °C was sufficiently long for the complete reduction of CuO to Cu by carrying out extensive metallographic examination. Additionally, the predicted weight reduction (T15, 22.1%) based on the binder content and loss of O by H reduction roughly matched experimentally measured weight reduction (24.3%), indirectly indicating that the reduction of CuO to Cu was completed. The mean size of the micropores on and within the walls was measured as 3.4 ± 2 µm and 9.0 ± 1 µm for the Cu foam without reduction pre-heat treatment (H1, Fig. 5a and c) and with reduction pre-heat treatment (H2, Fig. 5b and d), respectively. In addition, it is clear from the comparison between Fig. 5c (foam H1) and d (foam H2) that the fraction of micropores present on the surface of, and within, the walls of the Cu foams is much higher for foam H1 without the reduction pre-heat treatment. These micropores likely result from gas evolution (due to the burn-off of PVA and steam from the reduction of cupric oxide to Cu), and/or volume decrease from reduction and incomplete sintering. The high fraction of small, open micropores on and within the walls of foam H1 created without reduction pre-heat treatment may have adverse effects on the foam mechanical properties, since they could decrease the strength and stiffness of the walls. Conversely, the increased surface area provided by the micropores is beneficial to enhancing chemical reactions and/or heat transfer. Furthermore, more complete sintering enabled by the reduction pre-heat treatment used in foam H2 reduces the wall thickness (from 60 µm for H1 to 29 µm for H2) and increases the overall shrinkage of the foam (Table 1).

3.3. Effect of solidification speed

The casting temperature is varied from −30 to −10 °C in order to observe the effect of solidification speed on the morphology and structure of the pores and Cu walls in the foams T10–T30. Fig. 6(a–d) show optical micrographs of polished longitudinal cross-sections of these Cu foams solidified at a casting temperature of −10, −15, −20 and −30 °C, respectively. Fig. 6(a–d) suggest that the overall pore morphology is dependent upon the casting temperature. First, a denser region near the mold bottom exhibits pores that are non-directional due to rapid solidification, where the oxide powders are engulfed early by the ice front. As the casting temperature decreases (from Fig. 6(a)–(d)), the solidification speed increases and the height of the denser region with random pore structure increases, because the velocity of the ice front exceeds for a longer time the critical velocity at which the oxide particles become entrapped, rather than rejected, by the growing dendrites [34]. The region of equiaxed porosity near the mold bottom then transitions into a region of larger-sized lamellar, oriented pores. This change in pore structure (in orientation, shape and size) and the subsequent widening of the elongated pores as they extend away from the mold bottom are due to the freezing rate decreasing as heat removal becomes slower with higher growing ice front [15]. The large void

visible near the center of Fig. 6d is due to the cross-section plane being parallel to the pore walls in this particular region, and no void is observed in the micrographs of the other half of the same Cu foam along the radial direction. For the foams with a casting temperature of −10 and −15 °C, the initial shape of the green body is well maintained after the reduction and sintering processes, whereas for the foams cast at −20 and −30 °C, some degree of warping is observed after the reduction and sintering processes. This is probably because, for the later foams, the denser cellular region near the mold bottom shrinks differently than the more porous, lamellar region, resulting in internal stresses sufficient to deform the foam.

Fig. 7 shows plots of variations in the porosity, macropore width, and Cu wall width as a function of the casting temperature. For the three highest casting temperatures (−10, −15 and −20 °C), there is a clear trend of macropore width and wall width decreasing with decreasing casting temperature (i.e., with increasing freezing velocity), with the porosity remaining near constant at 67%. For the lowest casting temperature of −30 °C, both the macropore width and wall width remain almost unchanged as compared to −20 °C, with the porosity decreasing slightly from 67% to 63%. An inverse relationship between the Cu wall width and the velocity of the ice front has been reported previously [16]: with lower casting temperature, more numerous and thinner dendrites are created, leading to thinner lamellar macropore and wall widths, because ice nucleation is enhanced under higher supercooling conditions [17]. In the present experiments, this effect appears to saturate below −20 °C. According to an empirically obtained inverse relationship between the wall width (w) and ice front velocity (v) to the n power ($w \propto 1/v^n$ where n is a constant ranging from 1 to 4, [38]), both the wall width and macropore width are anticipated to initially decrease with decreasing casting temperature but eventually saturate at further decreased casting temperature, which is in agreement with the experimental trend of wall width and macropore width found in Fig. 7.

3.4. Effect of slurry powder content

The influence of powder volume fraction in the slurry is often considerable, particularly when the powders are nanometric, because nanoparticles tend to aggregate and form micro-clusters due to attractive van der Waals forces [35]. It is thus difficult to achieve a uniform dispersion of nanoparticles in a slurry. Although a low volume fraction of nanoparticles (less than 6 vol%) can be dispersed relatively easily, e.g., by using ultrasonic dispersion, a higher 'drag force' can prevent nanoparticles from being uniformly dispersed at higher volume fractions [36]. Particle interaction in the dispersed suspension can be described by the competition between the van der Waals force and the interfacial energy, which together determine the stability of a colloidal system. On the basis of the Derjaguin–Landau–Verwey–Overbeek (DLVO) theory [37], a colloidal suspension is stable when the repulsive force acting on the diffusive double electric layer is greater than the attractive (van der Waals) force between the particles. Thus, a homogeneous suspension for high volume fractions of nanosized powder is difficult to achieve, because the closer the particles are packed, the stronger their interactions [16,38]. Furthermore, powder volume fraction can also have a strong influence on the pore morphology. Shanti and coworkers [39] reported a "breakthrough" phenomenon, as the solid/liquid (ice/water) interface engulfs the particles and pure ice dendrites no longer form. Here, the threshold powder volume fraction, above which directional pores can no longer be formed, is defined as the "breakthrough concentration". A lower breakthrough concentration thus implies that the solid/liquid interface engulfs more easily the particles, thus resulting in non-directional pores, at which point, the osmotic pressure exceeds the capillary pressure [16,39]. The powder volume fraction of all samples used in this study does not appear to exceed the breakthrough concentration, resulting in directional pores in all cases, except at the very bottom of the samples where
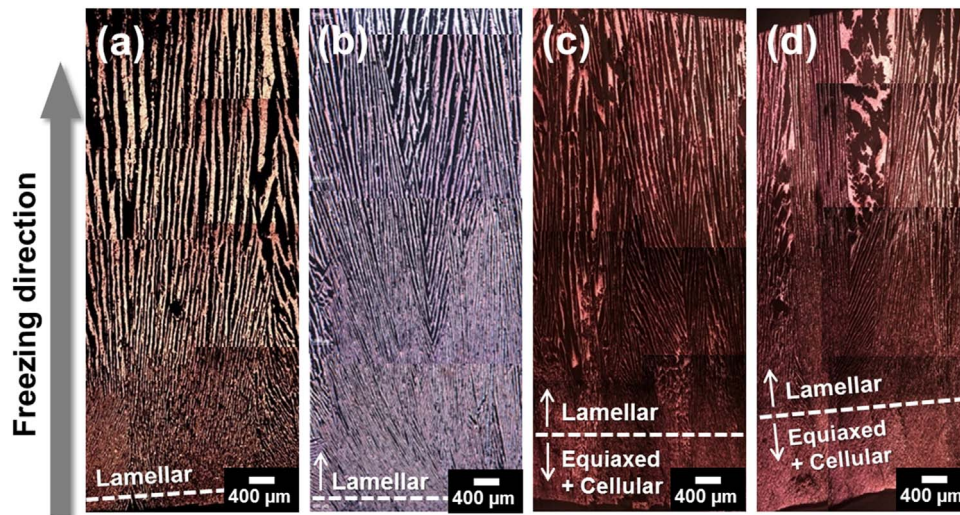
Fig. 6. Optical micrographs of longitudinal cross-sections of Cu foams created from slurries with 12.5 vol% oxide particles solidified at decreasing casting temperatures: (a) −10 (T10), (b) −15 (T15), (c) −20 (T20), and (d) −30 (T30) °C. The transition between a cellular region near mold bottom and a lamellar pore region is marked with a dotted line.
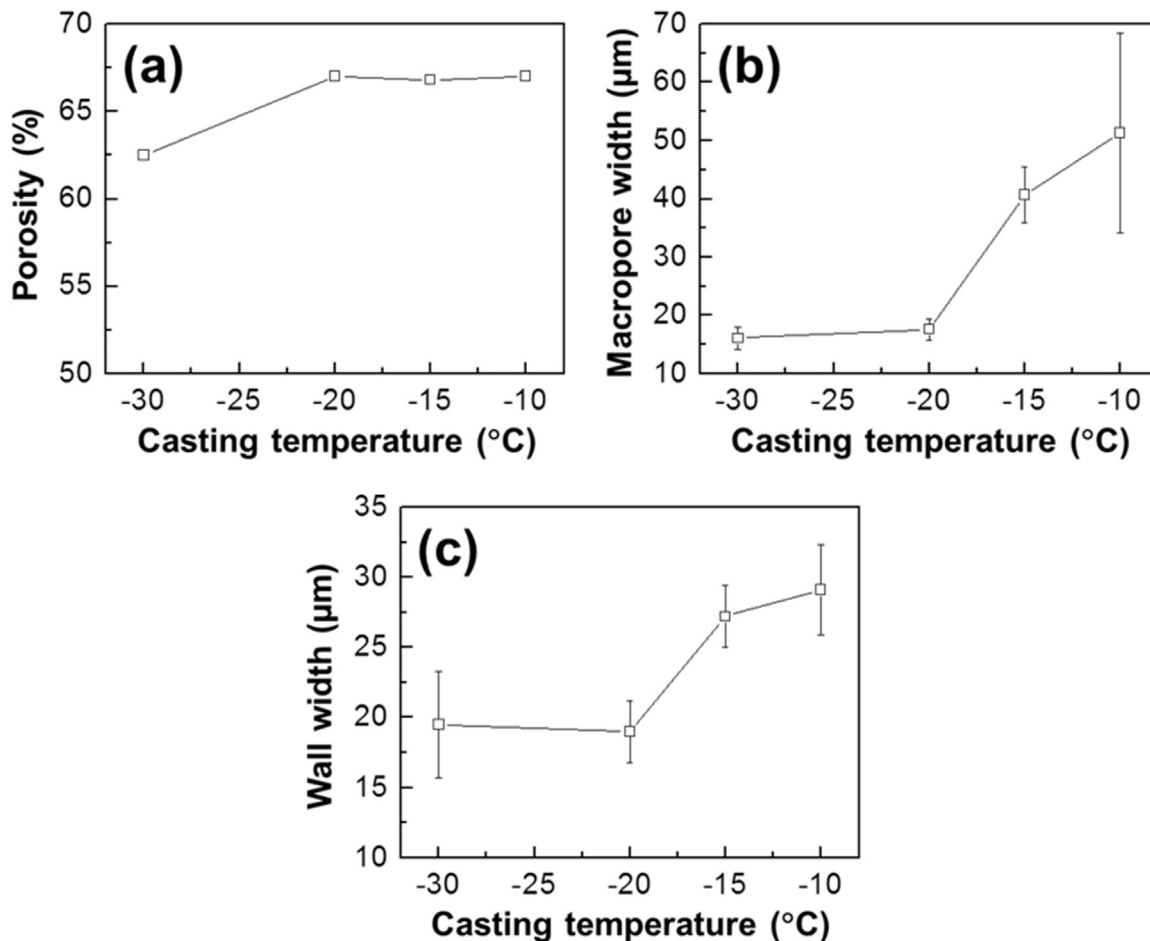

Fig. 7. Plots of (a) porosity, (b) macropore width, and (c) wall width against slurry casting temperature at constant slurry volume fraction of 12.5% (foams T10, T15, T20, and T30).

solidification was very rapid.

Fig. 8(a–f) show optical micrographs of radial (a–c) and longitudinal (d–f) cross-sections of foam V13, V16 and V19, created from slurries with 12.5, 16.0 and 19.2 vol% oxide powders respectively. It is apparent that, with increasing volume fraction of oxide powder in the slurry, the porosity and pore width decrease and the Cu wall width increases. This is expected, because with increasing slurry oxide content, more oxide particles are pushed in the interdendritic spaces and pure ice dendrites are thinner before they engulf the packed slurry in these spaces. As shown in Fig. 9(a–c), the porosity, macropore width, and Cu wall width are plotted against the slurry powder content. Both the porosity and macropore width indeed show near inversely linear relationship with the powder volume fraction (Fig. 9a and b), whereas the Cu wall width increases near linearly with the powder
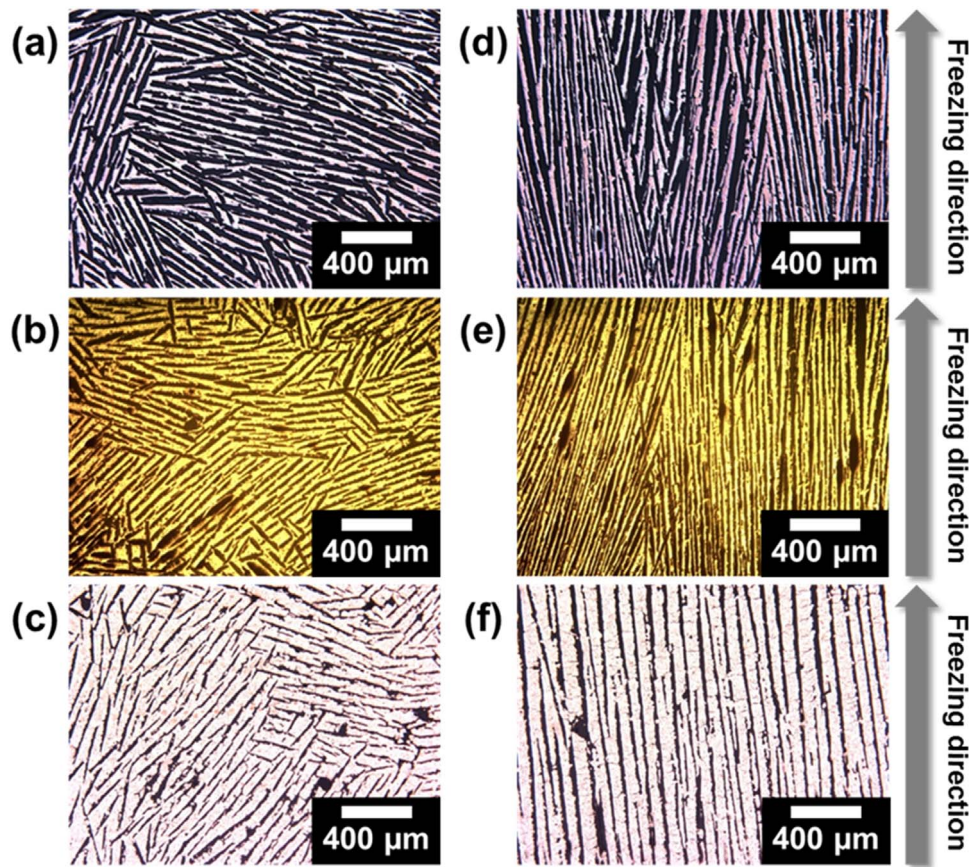
Fig. 8. Optical micrographs of (a–c) radial and (d–f) longitudinal cross-sections of center region of Cu foams solidified at −15 °C from slurries with increasing oxide powder fractions: (a, d) 12.5 vol% (foam V13), (b, e) 16.0 vol% (foam V16), and (c, f) 19.2 vol% (foam V19).

volume fraction (Fig. 9c). A similar trend is also observed in most other materials systems [40]. For example, in directionally solidified slurries of hydroxyapatite, bioactive glass and NiO-YSZ powders, and in a non-directionally solidified slurry of alumina powders, a higher powder fraction in the slurry also resulted in lower porosity [41–45]. Ran et al. [30] also reported a near linear decrease of porosity (from 50% to 31%) with increasing CuO powder fraction (from 20 to 40 vol%) in their non-directionally freeze-cast foams which were vacuum-decomposed to Cu and sintered at 900 °C for 2 h. No measurements of pore or wall sizes were reported in the above articles, but a recent review by Deville et al. [40] shows that the maximum compressive strength achievable in freeze-cast ceramics increases as pore size and porosity decrease.

3.5. Yield and plasticity behavior

Compressive stress-strain curves are shown in Fig. 10a for specimens of foams V13 (p=63%) with pore orientation parallel (V13P) and normal (V13N) to the load axis. The initial region of the curve corresponds to the linear elastic stage, ending with yield stresses of 43 and 14 MPa for the V13P and V13N samples, respectively. The Cu foams then experience a long plastic plateau where stress fluctuates, which ends with a steady stress increase due to densification at ~ 60% strain, followed by the final densification regime with steeply rising stresses; this behavior is typical of ductile metallic foams [18,19]. The Cu foam with pores normal to the loading axis yielded at about 1/3 of the yield stress of the Cu foam with pores parallel to the loading axis because bending is expected to be the major deformation mode of the walls in the former case, and plastic buckling in the latter. Nevertheless, the flow stress of the V13N foam sample becomes higher than that of the V13P foam sample after ~ 22% strain (Fig. 10a). The drop in stress for sample V13P from the yield strain (~1%) to a strain of

~40% is hypothesized to be due to plastic buckling of the longitudinally-loaded walls occurring cooperatively over large regions containing many parallel Cu walls (i.e., the prior ice dendrite colonies), resulting in zigzagged columns with increasing strain (observed by naked eye on some of the specimens); by contrast, only plastic bending of Cu walls takes place within the V13N foam sample [47].

The compressive yield strengths of the V13P and V13N Cu foam samples are plotted and compared with the predictions made by the Gibson and Ashby model (i.e., bending model) [48] and the simplified compressive model (i.e., compression model) both developed for foams with struts [19,49] as shown in Fig. 10b. Only a few studies have reported the compressive properties of pure Cu foam [47,50–52]. Among them, only the study on lotus Cu foams by Hyun et al. report foams with oriented, elongated pores similar to those in the present work [47]; these foams were created by directional solidification of liquid Cu saturated at high pressure with hydrogen, where aligned, elongated cylindrical pores are created by hydrogen rejection during solidification. Despite the higher porosity of the present powder-metallurgy Cu foams as compared to the solidified lotus Cu foams (p=63.0% vs. 59.5%), the yield strength of the ice-templated Cu foams is 3–4 times greater than that of the lotus Cu foams, although a larger number of samples should be tested and compared to draw a statistically meaningful conclusion. We can suggest several possible reasons for the much greater strength of our ice-templated Cu foams. First, the different processing methods could have resulted in considerable differences in Cu microstructure. Our Cu foams were created based via sintering of Cu powders created by in-situ reduction of CuO powders, whereas the lotus Cu foams were directionally cast from liquid Cu. Therefore, our powder-metallurgy Cu foams may contain some oxygen in solid solution and may exhibit finer grains with resultant increase in yield strength. Conversely, the cast lotus Cu foams
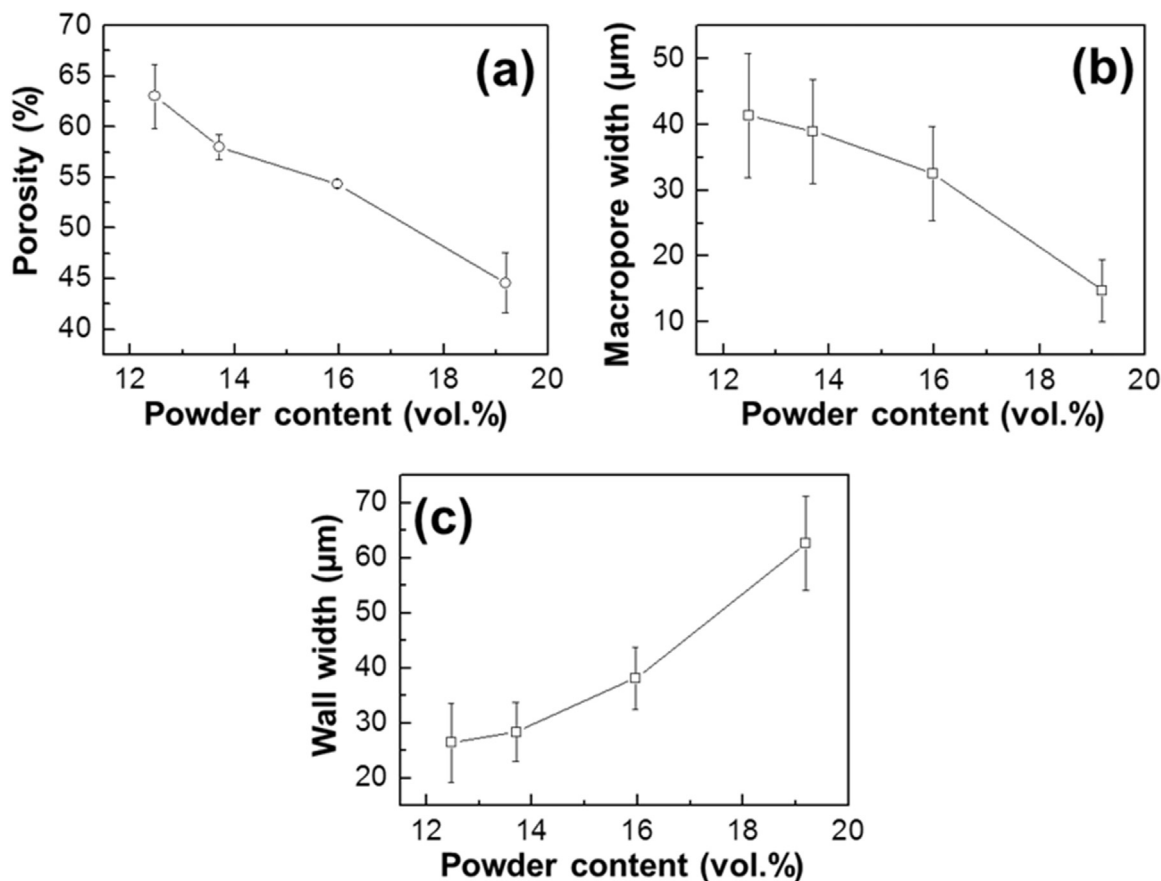
Fig. 9. Plots of (a) porosity, (b) macropore width, and (c) wall width against oxide powder content in slurry at constant casting temperature of −15 °C (foams V13, V14, V16, and V19).

are expected to be purer and have very coarse grains with resultant lower yield strength. Depending on the processing conditions, the yield strength of bulk Cu can increase by up to 22% with increasing oxygen content [53]. Taking the yield strength of oxygen-free bulk Cu as 176 MPa [46] and that of bulk Cu containing ~250 ppm oxygen as 215 MPa [53], we displayed the yield strength of our ice-templated Cu foams as ranges of short vertical lines as shown in Fig. 10b. Despite the slightly lowered relative yield strength values of our ice-templated Cu foams with the assumption of sufficient oxygen content, they are still far greater than those of the lotus Cu foams, suggesting that the oxygen solid-solution strengthening is not the dominant strengthening mechanism in our ice-templated Cu foams. Second, it might be explained by the large difference in pore width because the compressive strength decreases with increasing pore size at a given porosity [54,55]; despite much larger depth and height, the pore width (41 μm) of the ice-templated Cu foams is roughly an order of magnitude smaller than the diameter of the pores (356 μm) of the lotus Cu foams. Third, the difference in the cellular architecture of the foams may contribute to the difference in yield strength. The lotus Cu foam shows corrugated, interconnected walls while our Cu foam consists of flat walls connected occasionally by bridges between them. A further systematic study is required to identify the relative importance of the above mechanisms.

The yield strength, σ^* of open-cell metallic foams can be predicted by the Gibson and Ashby model, assuming that struts undergo bending deformation:

$$\frac{\sigma^*}{\sigma_{Cu}} = C_1 \left(\frac{\rho^*}{\rho_{Cu}} \right)^{3/2} \tag{1}$$

where C_1 is a constant generally equal to 0.3, and σ_{Cu} and ρ_{Cu} are the yield strength and the density of bulk Cu, taken as σ_{Cu}=176 MPa and ρ_{Cu}=8.96 g cm^{-3} [46]. The V13N Cu foam sample exhibits a yield

strength, which is in reasonable agreement with the value predicted by Eq. (1) (14 vs. 12 MPa), while the V13P Cu foam sample shows quadruple the value predicted by Eq. (1) (43 vs. 12 MPa).

A simplified compressive model is better suited for the parallel orientation, where it is assumed that parallel walls (or struts) surrounding the aligned macro-pores deform uniaxially:

$$\frac{\sigma^*}{\sigma_{Cu}} = C_2 \left(\frac{\rho^*}{\rho_{Cu}} \right) \tag{2}$$

where C_2 is a constant determined as 0.5. Based on the Eq. (2), the yield strength of the V13P Cu foam sample is quite similar to the predicted value (43 vs. 33 MPa). This thus indicates that the vertical walls in the V13P Cu foam sample, acting as compressive members connected by occasional perpendicular bridges enhancing buckling resistance, are likely to yield by uniaxial compression rather than bending [56]. Consequently, the compressive behavior of the Cu foams with elongated, parallel pores examined in this study is expected to be strongly anisotropic for all directions with respect to the loading axis, not solely for the two extreme example cases measured here.

3.6. Plastic energy absorption

The energy absorption of the directional Cu foams can be determined qualitatively from the integrated area under the stress-strain curve [48]:

$$W = \int_0^{\varepsilon_D} \sigma(\varepsilon) d\varepsilon \tag{3}$$

where W is the energy absorption per unit volume and ε_D is the densification strain, which is defined as the nominal strain value at which opposing cell walls start to come into contact and crush together [57]. Although the densification strain can be determined quantita-
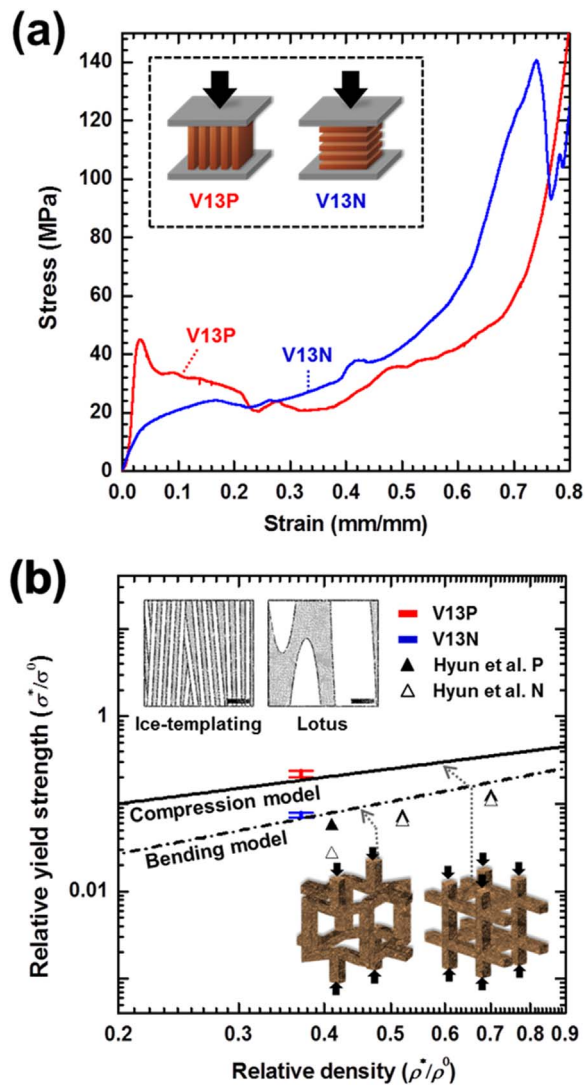
Fig. 10. (a) Compressive stress–strain curves of two Cu foams from specimen V13 (with 63% porosity) with porosity oriented parallel (labeled V13P) and normal (labeled V13N) to the compressive loading direction; (b) plot of relative yield strength (normalized by the yield strength of oxygen-fee bulk Cu, 176 MPa [46] and that of bulk Cu containing ~250 ppm oxygen, 215 MPa [53]) versus relative density comparing experimentally measured data and cellular model predictions. For comparison, the yield strength data for directional lotus Cu foams from literature are also plotted [47]. Shown also in upper inset are cross-sectional schematics of the ice-templated and lotus Cu foams; scale bar, 200 μm.

Table 2
Densification strain, corresponding stress, and absorption energy of Cu foams V13, compared to those of the previously reported directional lotus Cu foams by Hyun et al. [47] for the room-temperature compressive test.

	Porosity	Compressive direction	Densification strain, ε_D	Stress (MPa)	Absorbed energy (MJ/m^3)
V13	63%	**Parallel (P)**	**0.68**	**53**	**21**
		Normal (N)	**0.56**	**51**	**16**
Hyun et al. [47]	60%	Parallel (P)	0.46	92	28
		Normal (N)	0.33	36	7

63.0%). On the other hand, the energy absorption characteristic is considerably more isotropic for the ice-templated, sintered Cu foams than the cast, lotus Cu foams; the ratio of the energy absorption of the V13P and V13N Cu foam samples is 1.3, which is a third of the corresponding ratio (4.0) for the two cast lotus Cu foams, suggesting that our ice-templated, sintered Cu foams have promising potential for use in isotropic energy absorption applications, despite their marked yield strength anisotropy.

4. Conclusions

Cu foams were synthesized through a directional freeze-casting method where nanometric cupric oxide (CuO) powder in suspension within a aqueous slurry are rejected from growing columnar ice dendrites and are enriched in the interdendritic spaces. After freeze drying removal of the ice, reduction of the oxide to metallic copper (Cu) was carried out at 250 ℃, followed by sintering of the Cu particles at 800 ℃ under a hydrogen atmosphere, forming Cu walls surrounding elongated pores replicating the ice dendrites. This study investigated the effects of three important processing parameters on the morphology of the Cu foams:

1. In all samples subjected to the 250 ℃ /800 ℃ heat treatments, the Cu walls are well sintered and show few internal pores but high surface porosity. In one sample where the reduction pre-heat treatment at 250 ℃ was not carried out, the Cu walls exhibit within their volumes a high fraction of ~3 μm micropores, due to incomplete sintering. Consistent with the incomplete sintering, this sample exhibits wider lamellar macropores, wider Cu walls and less volumetric shrinkage.

2. With increasing powder fraction in the slurry, foams exhibit decreases in both macro-porosity and macropore width, and increase in Cu wall width. This is expected as, with increasing oxide powder fraction in the slurry, more oxide particles are pushed in the interdendritic spaces.

3. The casting temperature was varied between −10 and −30 ℃. Near the mold bottom surface, the velocity of the ice front exceeded the critical velocity, resulting in powders being engulfed between non-directional ice dendrites. Oriented, elongated macropores form farther from the mold bottom as solidification speed decreases, and the pore width and Cu wall width decrease with decreasing casting temperature, with the porosity maintained at 67%. This is perhaps because greater supercooling generally induces higher occurrence of ice nucleation.

4. Compressive tests were carried out on specimens of a Cu foam (p=63%) with the uniaxial loading direction parallel and perpendicular to the wall orientation. The yield strength is three-fold higher (43 vs. 14 MPa) when walls are oriented parallel to the loading axis. The compressive behavior of the Cu foam is well described by the strut compression model and the strut bending models, Eqs. (2) and (1), for the parallel and normal cases, respectively. In terms of plastic energy absorption capacity of our Cu foam samples are

tively from each stress-strain curve using the 'efficiency' technique developed by Tan et al. [58], to ensure fair comparison we defined it as the strain value at which the slope of the stress-strain curve increases steeply after the stress plateau region as was defined in the paper by Hyun et al. [47].

From the compressive stress-strain curve, we measured the absorbed energy up to the densification strain by using Eq. (3). In Table 2, the densification strain, stress, and energy absorption values of the two types of the ice-templated, sintered Cu foams are displayed and compared with those of the cast, lotus Cu foams [47]. As seen from the stress-strain curves in Fig. 10a, the V13P Cu foam sample shows ~ 37% higher energy absorption than that of the V13N Cu foam sample (21 vs. 16 MJ m^{-3}, p=63%), primarily because the V13P Cu foam sample has much higher yield strength (σ*, 43 vs. 14 MPa) and larger densification strain (ε_D, 0.68 vs. 0.56) than the V13N Cu foam sample. Furthermore, the calculated absorbed energies of the V13P and V13N Cu foam samples are comparable to those reported for the cast lotus Cu foams (Table 2), despite the lower porosity of the Cu foams (p=59.5 vs.

comparable to those reported for the cast lotus Cu foams, despite our foam's higher porosity (p=63 vs. 59.5%). The energy absorption is considerably less anisotropic for our Cu foams than the cast, lotus Cu foams: the ratios of the energy absorptions along the parallel and perpendicular directions are 1.3 and 4.0 for our Cu foams and the lotus Cu foams, respectively.

With their directional macropores between cellular walls and equiaxed micropores within walls and at their surfaces, freeze-cast Cu foams are candidates for anode current collector in lithium ion batteries, where the foam porous structure is expected to effectively accommodate the volume expansion/contraction during (de)lithiation. Furthermore, the aligned macropores increase permeability and thus may facilitate ionic mass transfer during the charging/discharging process. The foam's ductile behavior in compression, and their high strength and plastic energy absorption also makes them attractive for batteries (e.g. during impact) and for other structural applications where the high thermal and electrical conductivity of Cu are desirable.

Acknowledgments

References

[1] P.K. Khanna, S. Gailkwad, P.V. Adhyapak, N. Singh, R. Marimuthu, Synthesis and characterization of copper nanoparticles, Mater. Lett. 61 (2007) 4711–4714.

[2] A.I. Cuba-Ramos, D.C. Dunand, Preparation and characterization of directionally freeze-cast copper foams, Metals 2 (2012) 265–273.

[3] L. Xue, Z. Fu, Y. Yao, T. Huang, A. Yu, Three-dimensional porous Sn–Cu alloy anode for lithium-ion batteries, Electrochim. Acta 55 (2010) 7310–7314.

[4] P. Chladek, E. Croiset, W. Epling, R.R. Hudgins, Characterization of copper foam as catalytic material in ethanol dehydrogenation, Can. J. Chem. Eng. 85 (2007) 917–924.

[5] A. Siahpush, J. O'Brien, J. Crepeau, Phase change heat transfer enhancement using copper porous foam, J. Heat. Transf. 130 (082301) (2008) 1–11.

[6] J. Xu, X. Ji, W. Zhang, G. Liu, Pool boiling heat transfer of ultra-light copper foam with open cells, Int. J. Multiphas. Flow. 34 (2008) 1008–1022.

[7] S. Sen, D. Liu, G.T.R. Palmore, Electrochemical reduction of CO_2 at copper nanofoams, ACS Catal. 4 (2014) 3091–3095.

[8] G. Avgouropoulos, J. Papavasiliou, M.K. Daletou, J.K. Kallitsis, T. Ioannides, S. Neophytides, Reforming methanol to electricity in a high temperature PEM fuel cell, Appl. Catal. B-Environ. 90 (2009) 628–632.

[9] Y. Li, S. Chang, X. Liu, J. Huang, J. Yin, G. Wang, D. Cao, Nanostructured CuO directly grown on copper foam and their supercapacitance performance, Electrochim. Acta 85 (2012) 393–398.

[10] X. Xiao, P. Zhang, M. Li, Preparation and Thermal characterization of paraffin/ metal foam composite phase change material, Appl. Energy 112 (2013) 1357–1366.

[11] M.S. Aly, A. Almajid, S. Nakano, S. Ochiai, Fracture of open cell copper foams under tension, Mater. Sci. Eng. A 519 (2009) 211–213.

[12] S. Nam, H. Jo, H. Choe, D. Ahn, H. Choi, Development of nanoporous copper foams by chemical dealloying of mechanically alloyed Al–Cu compounds, Mater. Trans. 55 (2014) 1414–1418.

[13] H. Park, C. Ahn, H. Jo, M. Choi, D. Kim, D. Kim, S. Jeon, H. Choe, Large-area metal foams with highly ordered sub-micrometer-scale pores for potential applications in energy areas, Mater. Lett. 129 (2014) 174–177.

[14] J. Kim, R. Kim, H. Kwon, Preparation of copper foam with 3-dimensionally interconnected spherical pore network by electrodeposition, Electrochem. Commun. 10 (2008) 1148–1151.

[15] S. Deville, E. Saiz, A.P. Tomsia, Freeze casting of hydroxyapatite scaffolds for bone tissue engineering, Biomaterials 27 (2006) 5480–5489.

[16] S. Deville, Freeze-casting of porous ceramics: a review of current achievements and issues, Adv. Eng. Mater. 10 (2008) 155–169.

[17] W.L. Li, K. Lu, J.Y. Walz, Freeze casting of porous materials: review of critical factors in microstructure evolution, Int. Mater. Rev. 57 (2012) 37–60.

[18] Y. Chino, D.C. Dunand, Directionally freeze-cast titanium foam with aligned, elongated pores, Acta Mater. 56 (2008) 105–113.

[19] J.C. Li, D.C. Dunand, Mechanical properties of directionally freeze-cast titanium foams, Acta Mater. 59 (2011) 146–158.

[20] J.L. Fife, J.C. Li, D.C. Dunand, P.W. Voorhees, Morphological analysis of pores in directionally freeze-cast titanium foams, J. Mater. Res. 24 (2009) 117–124.

[21] R. Sepúlveda, A.A. Plunk, D.C. Dunand, Microstructure of Fe_2O_3 scaffolds Created by freeze-casting and sintering, Mater. Lett. 142 (2015) 56–59.

[22] A. Röthlisberger, S. Häberli, R. Spolenak, D.C. Dunand, Synthesis, structure and mechanical properties of directionally freeze-cast tungsten foams, J. Mater. Res. 31 (6) (2016) 753–764.

[23] J.H. Um, H.J. Park, Y.H. Cho, M.P.B. Glazer, D.C. Dunand, H.M. Choe, Y.E. Sung, 3D interconnected SnO2-coated Cu foam as a high-performance anode for lithium-ion battery applications, RSC Adv. 4 (2014) 58059–58063.

[24] H. Shin, M. Liu, Copper foam structures with highly porous nanostructured walls, Chem. Mater. 16 (2004) 5460–5464.

[25] S. Gao, S. Yang, J. Shu, S. Zhang, Z. Li, K. Jiang, Green fabrication of hierarchical CuO hollow micro/nanostructures and enhanced performance as electrode materials for lithium-ion batteries, J. Phys. Chem. C 112 (2008) 19324–19328.

[26] J.Y. Xiang, J.P. Tu, Y.Q. Qiao, X.L. Wang, J. Zhang, D. Zhang, C.D. Gu, Electrochemical impedance analysis of a hierarchical CuO electrode composed of self-assembled nanoplates, J. Phys. Chem. C 115 (2011) 2505–2513.

[27] W. Wang, R. Epur, P.N. Kumta, Vertically aligned silicon/carbon nanotube (VASCNT) arrays: hierarchical anodes for lithium-ion battery, Electrochem. Commun. 13 (2011) 429–432.

[28] B. Liu, J. Zhang, X. Wang, G. Chen, D. Chen, C. Zhou, G. Shen, Hierarchical three-dimensional ZnCo2O4 nanowire arrays/carbon cloth anodes for a novel class of high-performance flexible lithium-ion batteries, Nano Lett. 12 (2012) 3005–3011.

[29] K. Zhu, N.R. Neale, A. Miedaner, A.J. Frank, Enhanced charge-collection efficiencies and light scattering in dye-sensitized solar cells using oriented TiO_2 nanotubes arrays, Nano Lett. 7 (2007) 69–74.

[30] H. Ran, P. Feng, Z. Liu, X. Wang, J. Niu, H. Zhang, Complex-shaped porous Cu bodies fabricated by freeze-casting and vacuum sintering, Metals 5 (2015) 1821–1828.

[31] V.F. Petrenko, R.W. Whitworth, Physics of Ice, Oxford University Press, New York, 2002.

[32] K. Nagashima, Y. Furukawa, Nonequilibrium effect of anisotropic interface kinetics on the directional growth of ice crystals, J. Cryst. Growth 171 (1997) 577–585.

[33] G.W. Young, S.H. Davis, K. Brattkus, Anisotropic interface kinetics and tilted cells in unidirectional solidification, J. Cryst. Growth 83 (1987) 560–571.

[34] S. Deville, E. Saiz, A.P. Tomsia, Ice-templated porous alumina structures, Acta Mater. 55 (2007) 1965–1974.

[35] Y. Min, M. Akbulut, K. Kristiansen, Y. Golan, J. Israelachvili, The role of interparticle and external forces in nanoparticle assembly, Nat. Mater. (7) (2008) 527–538.

[36] L.Y. Chen, J.Q. Xu, H. Choi, M. Pozuelo, X. Ma, S. Bhowmick, J.M. Yang, S. Mathaudhu, X.C. Li, Processing and Properties of magnesium containing a dense uniform dispersion of nanoparticles, Nature 528 (2015) 539–543.

[37] W. Li, H. Zhang, Y. Jin, M. Gu, Rapid coagulation of silicon carbide slurry via direct coagulation casting, Ceram. Int. 30 (2004) 411–416.

[38] U.G.K. Wegst, M. Schecter, A.E. Donius, P.M. Hunger, Biomaterials by freeze casting, Philos. Trans. R. Soc. A 368 (2010) 2099–2121.

[39] N.O. Shanti, K. Araki, J.W. Halloran, Particle redistribution during dendritic solidification of particle suspensions, J. Am. Ceram. Soc. 89 (2006) 2444–2447.

[40] S. Deville, S. Meille, J. Seuba, A meta-analysis of the mechanical properties of ice-templated ceramics and metals, Sci. Technol. Adv. Mater. 16 (2015) 043501.

[41] S. Deville, Freeze-casting of porous biomaterials: structure, properties and opportunities, Materials (3) (2010) 1913–1927.

[42] A. Macchetta, I.G. Turner, C.R. Bowen, Fabrication of HA/TCP scaffolds with a graded and porous structure using a camphene-based freeze-casting method, Acta Biomater. 5 (2009) 1319–1327.

[43] K.K. Mallick, Freeze casting of porous bioactive glass and bioceramics, J. Am. Ceram. Soc. 92 (2009) S85–S94.

[44] J.W. Moon, H.J. Hwang, M. Awano, K. Maeda, Preparation of NiO–YSZ tubular support with radially aligned pore channels, Mater. Lett. 57 (2003) 1428–1434.

[45] S.W. Sofie, F. Dogan, Freeze casting of aqueous alumina slurries with glycerol, J. Am. Ceram. Soc. 84 (2001) 1459–1464.

[46] E.A. Brandes, G.B. Brook, Smithells Metals Reference Book, 7th ed., Butterworth-Heinemann, USA, 1992.

[47] S.K. Hyun, H. Nakajima, Anisotropic compressive properties of porous copper produced by unidirectional solidification, Mater. Sci. Eng. A 340 (2003) 258–264.

[48] L.J. Gibson, M.F. Ashby, Cellular Solids: Structures and Properties, Cambridge University Press, NY, 1997.

[49] E. Hong, B.Y. Ahn, D. Shoji, J.A. Lewis, D.C. Dunand, Microstructure and mechanical properties of reticulated titanium scrolls, Adv. Eng. Mater. 13 (2011) 1122–1127.

[50] A.E. Simone, L.J. Gibson, The compressive behaviour of porous copper made by the GASAR process, J. Mater. Sci. 32 (1997) 451–457.

[51] E. Zhang, B. Wang, On the compressive behaviour of sintered porous coppers with low to medium porosities-Part I: experimental study, Int. J. Mech. Sci. 47 (2005) 744–756.

[52] H. Nakajima, S.K. Hyun, K. Ohashi, K. Ota, K. Murakami, Fabrication of porous copper by unidirectional solidification under hydrogen and its properties, Colloids Surf. A 179 (2001) 209–214.

[53] D. Gusković, D. Marković, S. Nestorović, Effect of deformation and oxygen content on mechanical properties of different copper wires, Bull. Mater. Sci. 20 (5) (1997) 693–697.

[54] J. Bin, W. Zejun, Z. Naiqin, Effect of pore size and relative density on the mechanical properties of open cell aluminum foams, Scr. Mater. 56 (2007) 169–172.

[55] C.E. Wen, Y. Yamada, K. Shimojuma, Y. Chino, H. Hosokawa, M. Mabuchi, Compressibility of porous magnesium foam: dependency on porosity and pore size, Mater. Lett. 58 (2004) 357–360.

[56] S. Deville, E. Saiz, R.K. Nalla, A.P. Tomsia, Freezing as a path to build complex composites, Science 311 (2006) 515–518.

[57] P.J. Tan, S.R. Reid, J.J. Harrigan, On the dynamic mechanical properties of open-cell metal foams – a re-assessment of the 'simple-shock theory', Int. J. Solids Struct. 49 (2012) 2744–2753.

[58] P.J. Tan, J.J. Harrigan, S.R. Reid, Inertial effects in the uniaxial dynamic compression of a closed-cell aluminium alloy foam, Mater. Sci. Technol. 18 (2002) 480–488.